Journal of Computational Physics 473 (2023) 111724

Contents lists available at ScienceDirect

Journal of Computational Physics

www.elsevier.com/locate/jcp

Parallel computation of Inverse Compton Scattering radiation spectra based on Liénard-Wiechert potentials

Yi-Kai Kan [a,b], Franz X. Kärtner [a,b], Sabine Le Borne [c,*], Daniel Ruprecht [c], Jens-Peter M. Zemke [c]

[a] Center for Free-Electron Laser Science, Deutsches Elektronen-Synchrotron DESY, Notkestraße 85, 22607 Hamburg, Germany
[b] Department of Physics, University of Hamburg, Luruper Chaussee 149, 22761 Hamburg, Germany
[c] Hamburg University of Technology, Institute of Mathematics, Am Schwarzenberg-Campus 3, 21073 Hamburg, Germany

ARTICLE INFO

Article history:
Received 15 August 2021
Accepted 22 October 2022
Available online 28 October 2022

Keywords:
Liénard-Wiechert field
Radiation spectra
Inverse Compton Scattering

ABSTRACT

Inverse Compton Scattering (ICS) has gained much attention recently because of its promise for the development of table-top-size X-ray light sources. Precise and fast simulation is an indispensable tool for predicting the radiation property of a given machine design and to optimize its parameters. Instead of the conventional approach to compute radiation spectra which directly evaluates the discretized Fourier integral of the Liénard-Wiechert field given analytically (referred to as the frequency-domain method), this article focuses on an approach where the field is recorded along the observer time on a uniform time grid which is then used to compute the radiation spectra after completion of the simulation, referred to as the time-domain method. Besides the derivation and implementation details of the proposed method, we analyze possible parallelization schemes and compare the parallel performance of the proposed time-domain method with the frequency-domain method. We will characterize scenarios/conditions under which one method is expected to outperform the other.

1. Introduction

The most powerful X-ray sources today are Free-Electron Lasers (FEL) built at large national facilities producing intense, spatially coherent X-ray radiation [1,2]. FELs rely on magnetic undulators with periods on the order of 10 cm and therefore need highly relativistic beams to reach the hard X-ray regime. Inverse Compton scattering (ICS) instead uses an optical undulator, i.e., a counter propagating laser pulse, and therefore needs only weakly relativistic beams for hard X-ray production. ICS sources have therefore drawn great attention over the last ten years because of the potential to allow for table-top-size hard X-ray light sources with a much improved performance [3,4] when compared to an X-ray tube, eventually approaching that of a second generation synchrotron [5]. Such X-ray light sources would greatly increase access to high brightness X-ray radiation for fast experimental turn-around rather than waiting many months for using the light-source provided by large national facilities [6] including international travel to these facilities. Structural biology, biomedical imaging and materials screening would greatly benefit from such developments [7].

* Corresponding author.
E-mail address: leborne@tuhh.de (S. Le Borne).

https://doi.org/10.1016/j.jcp.2022.111724

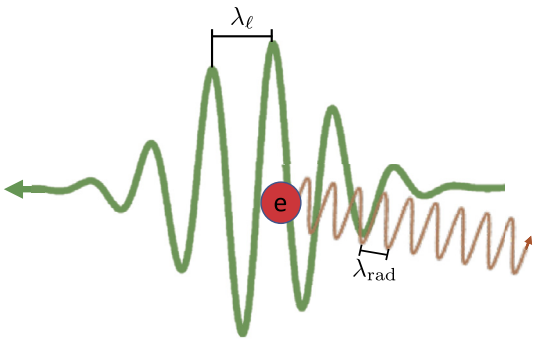

Fig. 1. Illustration of the ICS process. An electron (red circle) collides with a counter-propagating laser pulse (green line) of wavelength λ_ℓ and generates radiation (brown line) with shorter wavelength $\lambda_{\mathrm{rad}} = (1 + a_0^2/2)\lambda_\ell/4\gamma^2$. (For interpretation of the colors in the figure(s), the reader is referred to the web version of this article.)

In ICS, an electron bunch collides purposefully with a counter-propagating high-intensity laser pulse. The electrons are driven by the oscillating electrical field of the laser pulse to undergo a wiggling motion (Fig. 1). The radiation wavelength with maximum energy emitted from wiggling electrons is given by

$$\lambda_{\mathrm{rad}} = \frac{\lambda_\ell}{4\gamma^2}\left(1 + \frac{a_0^2}{2}\right)$$

where γ is the electron energy (normalized to its energy at rest), λ_ℓ is the laser wavelength and a_0 is the normalized vector potential characterizing the strength of the laser field [8]. As already discussed above, the counter-propagating laser pulse is often called an optical undulator with an equivalent period much shorter than that of magnetic undulators in conventional FELs. Thus, being able to achieve short wavelength radiation without a high-energy electron bunch driven by a large-scale accelerator is the major advantage of ICS sources.

Due to the increasing demand on developing ICS sources [7,9,26,10,6,11–14], numerical simulation is an indispensable tool to understand the generated radiation characteristics. To simulate the generated radiation, the Liénard-Wiechert field method is among the commonly used methods [15–19]. In this method, the radiation field is computed from the charged particle trajectories which are either given beforehand or solved in parallel during the simulation.

One of the challenges when computing radiation spectra generated by relativistic particles lies in the delay between the particle generating its contribution (retarded or emission time) and the observer detecting it (advanced time) which is not constant but depends on the distance between the particle and the observer at time of emission. Furthermore, to allow for a simple and quick computation of spectra via fast Fourier transform, it is preferable to have contributions at the observer on a uniform, equidistant time mesh. One possibility is to define a uniform mesh in the advanced time and then calculate the corresponding emission times ("retarded time scheme"). However, this approach is computationally expensive as it requires (numerical) root-finding and it is also memory intensive as full particle trajectories must be stored to allow interpolation to the computed emission times. By contrast, the advanced time scheme computes particle trajectories and emissions using a uniform time grid. At each time step, the corresponding advanced time is computed when the generated emission reaches the observer. This approach avoids computationally expensive root-finding but raises the new problem of how to deal with the different (non-uniform) advanced times at which the emissions reach the observer. Since one is typically interested in the amplitude $|E(x,\omega)|$ of the generated field in the frequency-domain [20] and not $E(x,t)$ itself, instead of first depositing contributions in physical space on a mesh and then applying a Fourier transform, it is possible to directly compute the amplitude that the particle contributes to each Fourier mode. This approach is commonly referred to as the frequency-domain method since it calculates directly the spectrum of the generated field but never the field itself [15,20]. However, as the computation of each Fourier mode is performed independently, this method intrinsically needs a high number of operations, i.e., $\mathrm{O}(N_\omega \cdot N_p \cdot N_s)$ where N_ω, N_p and N_s are the number of frequency points for the spectrum, the number of simulated particles and the number of simulation steps, respectively [20]. As an alternative, Sell et al. [21] use a time-domain approach where particle contributions at a given advanced time are interpolated to a uniform observer time mesh before being (Fourier) transformed to the frequency domain.

This method can benefit from the fast computation of the overall discrete spectrum using the Fast Fourier Transform (FFT) because the full sequence of interpolated fields over the observer time mesh is known. Thus, the time-domain method may have advantages in terms of computational time. This was pointed out in [20], however without a detailed analysis and verification.

In spite of the high computational cost, the frequency-domain method can be efficient in terms of memory cost when a large number of particles needs to be considered [20]. In this scenario, it may not be possible nor necessary to store the full history of all particle trajectories and the calculation of radiation spectra can be done in parallel to the calculation of particle trajectories in a simulation. To study real-world cases where a large number of particles and observation points are usually needed, the use of high-performance computers may be necessary [18,19].

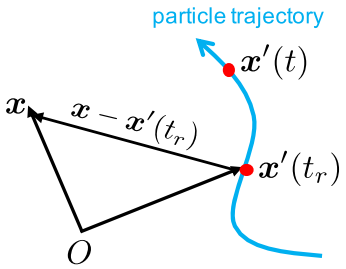

Fig. 2. Illustration of the retardation condition (2). Radiation emitted from a particle at time t_r at position $\boldsymbol{x}'(t_r)$ will arrive at the observer at position $\boldsymbol{x}$ at time t. The travel time of the radiation is $|\boldsymbol{x}-\boldsymbol{x}'(t_r)|/c_0$.

For the time-domain method, the superposition of particle fields relies on the interpolation onto a predefined uniform (advanced) time mesh. This implies that the particle information in some previous steps is needed when determining the superimposed field. In the implementation proposed by [20], the full history of the particle trajectories is available beforehand. Under this assumption, the computation of the particle trajectories is completely detached from the computation of the radiation field. However, for a simulation with a large number of particles, the storage of their trajectories needs an excessive memory capacity and such simulation may not be possible in practice. To mitigate the memory consumption for storing the particle trajectories, an algorithm which solves the particle trajectory and computes the superimposed field simultaneously might be necessary. One approach belonging to this category can be found in [21]. The particle trajectories are stored only for a certain number of preceding time steps in a so-called "ring buffer" [21] and used to interpolate the field onto a pre-defined uniform time grid. The drawback of this approach is that typically more field evaluations are performed (and stored) than are necessary for the interpolation.

In this article, we first describe the frequency-domain method to compute radiation spectra based on the Liénard-Wiechert potential. After that, we introduce our discretization and implementation of the time-domain approach and provide an analysis for two possible distributed parallelization schemes. In particular, the proposed algorithm needs to store the particle trajectories only for a single preceding time step. Finally, we propose and discuss a strategy for choosing parameters when applying the time-domain method and the frequency-domain method to compute ICS radiation spectra. Following this strategy, we analyze the performance of both methods and discuss the scenarios where one method outperforms the other. We conclude that the time-domain method is in general, i.e., within the specification of real-world experiment projects, more favorable than the frequency-domain method in terms of execution time in serial and in parallel when applied to compute the radiation spectra of an ICS process. Besides, we also show that the frequency-domain method can outperform the time-domain method in some circumstances.

2. Radiation calculation using Liénard-Wiechert fields

The radiation field that is emitted from a charged particle at position $\boldsymbol{x}'(t_r)$ at the (retarded) time t_r and observed at a fixed position $\boldsymbol{x}$ at time t (see Fig. 2) is given by the equations

$$\boldsymbol{E}(\boldsymbol{x},t)=\frac{1}{4\pi\varepsilon_0}\cdot\frac{q\boldsymbol{n}\times\left((\boldsymbol{n}-\boldsymbol{\beta}'(t_r))\times\dot{\boldsymbol{\beta}}'(\boldsymbol{t_r})\right)}{c_0(1-\boldsymbol{n}\cdot\boldsymbol{\beta}'(t_r))^3\,|\boldsymbol{x}-\boldsymbol{x}'(t_r)|},\qquad \boldsymbol{B}(\boldsymbol{x},t)=\frac{\boldsymbol{n}}{c_0}\times\boldsymbol{E}(\boldsymbol{x},t), \tag{1}$$

where $\boldsymbol{\beta}'\equiv\boldsymbol{x}'/c_0$ and $\dot{\boldsymbol{\beta}}'\equiv\ddot{\boldsymbol{x}}'/c_0$ denote the particle's velocity and acceleration (normalized by the speed of light c_0 in vacuum), q is the charge of the particle, ε_0 is the vacuum permittivity, defined by $\varepsilon_0\equiv 1/(\mu_0 c_0^2)$ for the vacuum permeability μ_0, and $\boldsymbol{n}\equiv(\boldsymbol{x}-\boldsymbol{x}')/|\boldsymbol{x}-\boldsymbol{x}'|$. (Compared to [22, Eqs. (14.13)+(14.14)], the velocity field (14.14) can be neglected in the radiation problem since the total power of the velocity field decays with the distance.) The observation time t and (retarded) emission time t_r fulfill the retardation condition (see Fig. 2)

$$t=t_r+\frac{|\boldsymbol{x}-\boldsymbol{x}'(t_r)|}{c_0}, \tag{2}$$

i.e., the radiation field generated at position $x'(t_r)$ at time t_r travels with the speed of light c_0 to reach the observation point $\boldsymbol{x}$, at $t=t_r+|\boldsymbol{x}-\boldsymbol{x}'(t_r)|/c_0$. There are some drawbacks when applying Eqns. (1), (2) to compute the radiation field:

- Root finding is needed to solve the retardation condition (2) for t_r which is computationally intensive [23].
- The trajectories of all particles have to be stored since they are required to compute the radiation field.
- In a numerical simulation, the electron trajectories are computed at discrete time points and interpolation is needed when t_r falls between two consecutive time points [23].

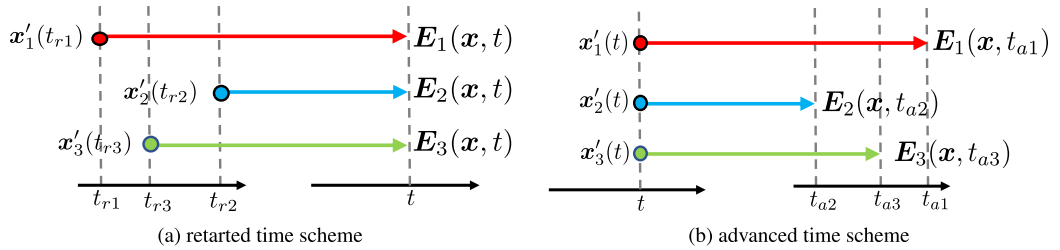

(a) retarted time scheme (b) advanced time scheme

Fig. 3. Illustration of (a) retarded time scheme and (b) advanced time scheme. Emission of radiation from three particles is considered and represented by different colors. To compute the field arriving at the observer $\boldsymbol{x}$ at time t from each particle in the retarded time scheme, we need to solve Eq. (2) for the retarded times t_{r1}, t_{r2} and t_{r3}. In the advanced time scheme, the particle trajectory at time t is used to compute the fields at advanced times t_{a1}, t_{a2} and t_{a3}, obtained by evaluating Eq (3) at which the observer at $\boldsymbol{x}$ receives the radiation field.

Alternatively, one may evaluate Eq. (1) at a future (advanced) time t_a,

$$t_a = t + \frac{|\boldsymbol{x} - \boldsymbol{x}'(t)|}{c_0}, \tag{3}$$

to obtain the field generated by an electron's motion at the current time t, using the substitutions $t \to t_a$ and $t_r \to t$. This scheme does not involve root-finding and we can compute the time t_a^k at which the radiation from particle k arrives at the observation position $\boldsymbol{x}$. However, as implied by Eq. (3), the arrival time of the radiation can be different for different particles and the superposition of particle fields is not straightforward. Both schemes are illustrated in Fig. 3.

When studying radiation phenomena, it is usually valid to consider the far-field approximation, that is the radiation field from a particle which is observed at a distance far from its position $|\boldsymbol{x}| \gg |\boldsymbol{x}'(t)|$, we have

$$|\boldsymbol{x} - \boldsymbol{x}'(t)| \approx |\boldsymbol{x}| - \boldsymbol{n} \cdot \boldsymbol{x}'(t)$$

where $\boldsymbol{n} \equiv \boldsymbol{x}/|\boldsymbol{x}|$, by abuse of notation, denotes an approximation of the normal vector $\boldsymbol{n} = (\boldsymbol{x} - \boldsymbol{x}'(t))/|\boldsymbol{x} - \boldsymbol{x}'(t)|$. The electric field and corresponding advanced time condition can be approximated accordingly,

$$\boldsymbol{E}(\boldsymbol{x}, t_a) \approx \frac{1}{4\pi\varepsilon_0} \cdot \frac{q\boldsymbol{n} \times \left((\boldsymbol{n} - \boldsymbol{\beta}'(t)) \times \dot{\boldsymbol{\beta}}'(t)\right)}{c_0(1 - \boldsymbol{n} \cdot \boldsymbol{\beta}'(t))^3 |\boldsymbol{x}|}, \tag{4}$$

for

$$t_a \approx t + \frac{|\boldsymbol{x}|}{c_0} - \frac{\boldsymbol{n} \cdot \boldsymbol{x}'(t)}{c_0}. \tag{5}$$

This approximation will be used throughout this article.

3. Frequency-domain method

One way to avoid the root-finding problem is to superimpose the fields at the observer in the frequency-domain. In a typical radiation study, one is interested in the spectral-angular distribution of the radiation [22, Eqn. (14.60)]

$$\frac{dI^2}{d\omega d\Omega} = \frac{2}{c_0\mu_0}|\boldsymbol{x}|^2 |\boldsymbol{E}(\boldsymbol{x}, \omega)|^2,$$

where ω is the frequency and Ω is the solid angle of the observation sphere surface with radius $|\boldsymbol{x}|$. The electric field in the frequency-domain is

$$\boldsymbol{E}(\boldsymbol{x}, \omega) \equiv \frac{1}{\sqrt{2\pi}} \int_{-\infty}^{\infty} \boldsymbol{E}(\boldsymbol{x}, t) \exp(j\omega t)\, dt \tag{6}$$

where $j \equiv \sqrt{-1}$.

By the superposition principle, the spectral-angular radiation distribution from a bunch of electrons is given by

$$\frac{dI^2}{d\omega d\Omega} = \frac{2}{c_0\mu_0}|\boldsymbol{x}|^2 \left| \sum_{k=1}^{N_p} \boldsymbol{E}_k(\boldsymbol{x}, \omega) \right|^2 \overset{(6)}{=} \frac{2}{c_0\mu_0}|\boldsymbol{x}|^2 \left| \sum_{k=1}^{N_p} \int_{-\infty}^{\infty} \frac{1}{\sqrt{2\pi}} \boldsymbol{E}_k(\boldsymbol{x}, t_a) \exp(j\omega t_a)\, dt_a \right|^2. \tag{7}$$

Substitution of Eq. (4) into Eq. (7), using the approximately constant observation direction $\boldsymbol{n} = \boldsymbol{x}/|\boldsymbol{x}|$, applying the variable transformation given in Eq. (5) (with $dt_a = (1 - \boldsymbol{n}\cdot\boldsymbol{\beta}_k'(t))\,dt$ by normalization of $\boldsymbol{\beta}_k' = \dot{\boldsymbol{x}}_k'/c_0$), and setting $\varepsilon_0 = (\mu_0 c_0^2)^{-1}$ in Eq. (7) results in [22, Eqn. (14.65)]

$$\begin{aligned}\frac{dI^2}{d\omega d\Omega}(\boldsymbol{n},\omega) &\approx \frac{q^2}{16\pi^3\varepsilon_0 c_0}\left|\sum_{k=1}^{N_p}\int_{-\infty}^{\infty}\underbrace{\frac{\boldsymbol{n}\times\left((\boldsymbol{n}-\boldsymbol{\beta}_k'(t))\times\dot{\boldsymbol{\beta}}_k'(t)\right)}{(1-\boldsymbol{n}\cdot\boldsymbol{\beta}_k'(t))^2}}_{\equiv\boldsymbol{\mathcal{A}}_k(\boldsymbol{n},t)}\frac{1}{(1-\boldsymbol{n}\cdot\boldsymbol{\beta}_k'(t))}\exp(j\omega t_a)\,dt_a\right|^2\\ &= \frac{q^2}{16\pi^3\varepsilon_0 c_0}\left|\sum_{k=1}^{N_p}\int_{-\infty}^{\infty}\boldsymbol{\mathcal{A}}_k(\boldsymbol{n},t)\exp\left(j\omega\left(t-\frac{\boldsymbol{n}\cdot\boldsymbol{x}_k'(t)}{c_0}\right)\right)dt\right|^2 \qquad (8)\\ &\text{with}\quad \boldsymbol{\mathcal{A}}_k(\boldsymbol{n},t) \equiv \frac{\boldsymbol{n}\times\left((\boldsymbol{n}-\boldsymbol{\beta}_k'(t))\times\dot{\boldsymbol{\beta}}_k'(t)\right)}{(1-\boldsymbol{n}\cdot\boldsymbol{\beta}_k'(t))^2}.\end{aligned}$$

In Eq. (8), it is the change of variables from t_a to t that circumvents the difficulty to superimpose the electrons' fields at asynchronous future time points. We have also dropped the common constant phase term $\exp(j\omega|\boldsymbol{x}|/c_0)$ in Eq. (8) as it has no impact on the overall amplitude. The time window of the simulation, i.e., when the acceleration of the charged particle by the driving field is nonzero, is chosen as $[0, t_{\text{end}}]$. We use an equidistant discretization in time with N_s intervals, $N_s\Delta t = t_{\text{end}}$, leading to

$$\frac{dI^2}{d\omega d\Omega}(\boldsymbol{n},\omega) \approx \frac{q^2(\Delta t)^2}{16\pi^3\varepsilon_0 c_0}\left|\sum_{k=1}^{N_p}\sum_{i=0}^{N_s}\boldsymbol{\mathcal{A}}_k(\boldsymbol{n},i\Delta t)\exp\left(j\omega\left(i\Delta t-\frac{\boldsymbol{n}\cdot\boldsymbol{x}_k'(i\Delta t)}{c_0}\right)\right)\right|^2. \qquad (9)$$

Introducing the abbreviations

$$\begin{aligned}\boldsymbol{\mathcal{E}}_{\boldsymbol{k,i}}(\boldsymbol{n},\omega) &\equiv \boldsymbol{\mathcal{A}}_k(\boldsymbol{n},i\Delta t)\exp\left(j\omega\left(i\Delta t-\frac{\boldsymbol{n}\cdot\boldsymbol{x}_k'(i\Delta t)}{c_0}\right)\right), \qquad (10)\\ \boldsymbol{\mathcal{E}}_i^{\text{bunch}}(\boldsymbol{n},\omega) &\equiv \sum_{k=1}^{N_p}\boldsymbol{\mathcal{E}}_{k,i}(\boldsymbol{n},\omega), \qquad \boldsymbol{\mathcal{E}}^{\text{sum}}(\boldsymbol{n},\omega) \equiv \sum_{i=1}^{N_s}\boldsymbol{\mathcal{E}}_i^{\text{bunch}}(\boldsymbol{n},\omega),\end{aligned}$$

and exchanging the order of summation w.r.t. k and i in (9), we obtain

$$\frac{dI^2}{d\omega d\Omega}(\boldsymbol{n},\omega) \approx \frac{q^2(\Delta t)^2}{16\pi^3\varepsilon_0 c_0}\left|\sum_{i=1}^{N_s}\sum_{k=1}^{N_p}\boldsymbol{\mathcal{E}}_{k,i}\right|^2 = \frac{q^2(\Delta t)^2}{16\pi^3\varepsilon_0 c_0}\left|\sum_{i=1}^{N_s}\boldsymbol{\mathcal{E}}_i^{\text{bunch}}\right|^2 = \frac{q^2(\Delta t)^2}{16\pi^3\varepsilon_0 c_0}\left|\boldsymbol{\mathcal{E}}^{\text{sum}}\right|^2.$$

A pseudocode for the frequency-domain method is provided in Algorithm 1.

Algorithm 1: Frequency-Domain Method.

```
Initialization:
    E^sum(n, ω) ← 0
for simulation step i do
    E_i^bunch(n, ω) ← 0
    for particle k do
        update trajectory
        E_i^bunch(n, ω) ← E_i^bunch(n, ω) + E_{k,i}(n, ω)
    E^sum(n, ω) ← E^sum(n, ω) + E_i^bunch(n, ω)
```

4. Time-domain method

To start our discussion, we first present the result of a test simulation for 10 particles initially at rest with random initial positions which are samples from a Gaussian distribution with mean 0 and standard deviation 1 in each direction. The particles are driven by a sinusoidal electromagnetic plane wave. In the simulation, the equations of motion for charged particles are simulated using the Boris method [24], and the trajectory of each particle is used to evaluate the radiation field arriving at an observation point and the corresponding observation time by evaluating Eq. (4) and Eq. (5).

The result of this trial simulation is shown in Fig. 4. Fig. 4(a) shows the E_y component of the radiation field generated by each particle. Fig. 4(b) shows a zoom-in view of Fig. 4(a). From the result of this trial simulation, we summarize the following observations:

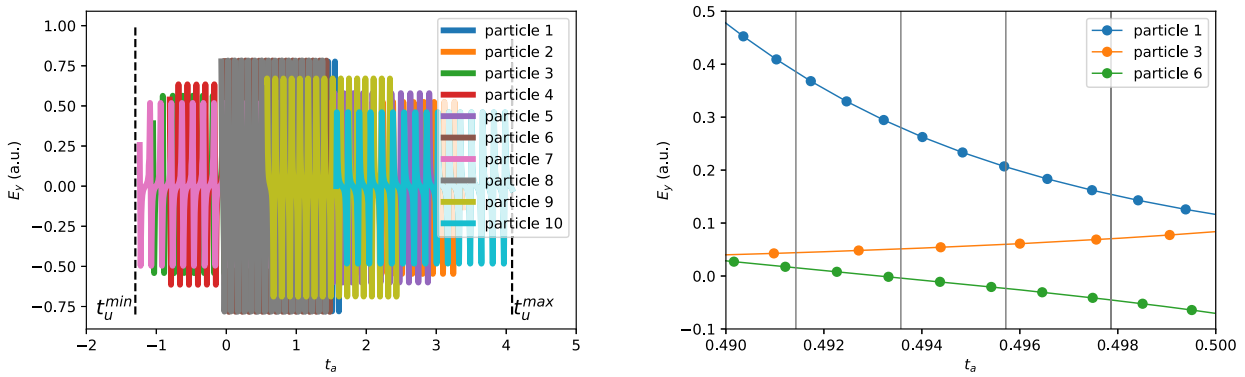

(a) radiation fields of all particles

(b) zoom-in for three selected particles

Fig. 4. Simulation result for the test simulation. (a) shows the temporal profiles of the radiation fields from all particles. (b) shows the zoom-in view of (a) for three selected particles. Here, the relative arrival time of particle radiation field is demonstrated instead of the absolute arrival time.

- The observed pulse duration of the radiation fields generated by the particles is different. This is illustrated in Fig. 4(a) and explained by Eq. (5),

$$\int dt_a^k = \int_{t_{\text{start}}}^{t_{\text{end}}} \left(1 - \boldsymbol{n} \cdot \boldsymbol{\beta}_k'(t)\right) dt = t_a^k(t_{\text{end}}) - t_a^k(t_{\text{start}}).$$

  Each particle moves at different phase of the external electromagnetic wave, and the particle velocities $\boldsymbol{\beta}_k'(t)$ driven by the external field during the simulation can be different. Therefore, the resulting integrals of dt_a^k are different for the particles.
- It is problematic to superimpose the fields of all particles since the radiation fields from the trajectories of different particles evaluated at the same time t are observed at different future times $t_a^k =\approx t + |\boldsymbol{x}|/c_0 - (\boldsymbol{n} \cdot \boldsymbol{x}_k'(t))/c_0$ (5). This is illustrated in Fig. 4(b).
- To superimpose the radiation fields, we define a uniform time grid $\boldsymbol{t}_u$ (indicated by the gray vertical lines in Fig. 4b) and interpolate the particles' fields to the uniform grid (details on the interpolation will follow in subsection 4.1).
- To cover the radiation temporal profile of all particles, we need to determine the upper and lower bound (annotated by $t_u^{\max}$ and $t_u^{\min}$ in Fig. 4a) of the uniform time grid $\boldsymbol{t}_u$.

To create a uniform time grid for the radiation field interpolation, we need to know the bound of the radiation temporal profile at different observation positions. For a simulation with N_p particles and N_{obs} observers, we determine the bounds of the uniform (advanced) time grid by

$$t_u^{\min} = \min\left\{t_a^{k,m}(t_{\text{start}}) \mid k = 1, \ldots, N_p,\ m = 1, \ldots, N_{\text{obs}}\right\}, \tag{11}$$

$$t_u^{\max} = \max\left\{t_a^{k,m}(t_{\text{end}}) \mid k = 1, \ldots, N_p,\ m = 1, \ldots, N_{\text{obs}}\right\}, \tag{12}$$

where $t_{\text{start}}, t_{\text{end}}$ denote the start/end of the simulation and

$$t_a^{k,m}(t) \approx t + \frac{|\boldsymbol{x}_m|}{c_0} - \frac{\boldsymbol{n}_m \cdot \boldsymbol{x}_k'(t)}{c_0}.$$

($|\boldsymbol{x}_m|$ is the same for all m observers since they are located on a spherical surface.) The lower bound $t_u^{\min}$ can be easily determined at the beginning of the simulation since we already have the initial positions of all particles. To determine the upper bound $t_u^{\max}$, it might be possible to perform a trial simulation in which we only compute the particles' trajectories and evaluate $t_u^{\max}$ by Eq. (12) at the end of trial simulation. However, this will become costly when N_p is large. To avoid such a trial simulation, we determine $t_u^{\max}$ by estimating the total radiation pulse duration from a particle bunch as follows.

As can be observed from Fig. 4(a), the total radiation pulse duration from all particles is influenced by the radiation pulse durations of single particles and the different lags in their arrival times. For the ICS problem, the radiation pulse duration from a single particle

$$T_{\text{rad}} \equiv \int dt_a = \int_0^{T_{\text{laser}}} \left(1 - \boldsymbol{n} \cdot \boldsymbol{\beta}'(t)\right) dt,$$

Table 1
Theoretical estimation of T_u by Eq. (16) for different parameter settings in comparison with results from trial simulations for the particles' trajectories using Eqs. (11), Eq. (12). Here, all length and time quantities are normalized to $2\pi/\lambda_0$ and $2\pi c_0/\lambda_0$, respectively, with $\lambda_0 = 1000$ µm.

$l_{b,x}$	$l_{b,y}$	$l_{b,z}$	T_{laser}	γ	$T_{\text{rad}}^{\text{bunch}}$ (15)	T_{rad} (13)	T_u (theory)	T_u (simulation)
10	10	10	10	40	35.0000	0.003125	35.0031	35.0211
20	10	10	10	40	35.8333	0.003125	35.8365	35.8876
10	20	10	10	40	35.8333	0.003125	35.8365	35.8540
10	10	20	10	40	68.3333	0.003125	68.3365	68.3328
10	10	10	20	40	35.0000	0.006250	35.0063	35.0310

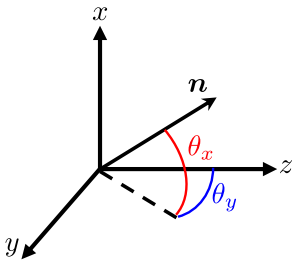

Fig. 5. Definition of the normal vector $\boldsymbol{n}$ pointing from the particle to the observer. θ_x is the angle between $\boldsymbol{n}$ and its projection to the y-z plane. θ_y is the angle between the z-axis and the projection of $\boldsymbol{n}$ to the z-y plane.

can be approximated for highly relativistic particles by

$$T_{\text{rad}} \approx \frac{T_{\text{laser}}}{2\gamma^2} \tag{13}$$

where $T_{\text{laser}} = t_{\text{end}} - t_{\text{start}}$ is the pulse duration of the counter propagating laser pulse. The maximum difference in arrival times of the radiation pulses from different particles is caused by their distribution in space and can be estimated by the last term of Eq. (5),

$$T_{\text{rad}}^{\text{bunch}} \equiv \max_{\theta_x,\theta_y} \max_{i,j=1,\dots,N_p} \left| \frac{\boldsymbol{n}\cdot(\boldsymbol{x}_i' - \boldsymbol{x}_j')}{c_0} \right|, \quad \text{where} \quad \boldsymbol{n} \equiv (\sin\theta_x, \cos\theta_x \sin\theta_y, \cos\theta_x \cos\theta_y). \tag{14}$$

θ_x and θ_y are the angles defining the observers' positions on the sphere (see Fig. 5). In the highly relativistic scenario, the opening angle of the radiation from a particle is of the order of $1/\gamma \ll 1$. We hence use approximations $\sin\theta \approx \theta$, $\cos\theta \approx 1$, and Eq. (14) becomes

$$T_{\text{rad}}^{\text{bunch}} \approx \max_{\substack{i,j=1,\dots,N_p \\ |\theta_x|,\,|\theta_y|<1/\gamma}} \left| \frac{\theta_x(x_i' - x_j') + \theta_y(y_i' - y_j') + (z_i' - z_j')}{c_0} \right|,$$

which has the upper bound

$$T_{\text{rad}}^{\text{bunch}} \lessapprox \frac{l_{b,x}}{\gamma c_0} + \frac{l_{b,y}}{\gamma c_0} + \frac{l_{b,z}}{c_0}, \tag{15}$$

where $l_{b,x}$, $l_{b,y}$ and $l_{b,z}$ denote the size of the particle bunch in each direction at t_{start}.

Thus, to cover the total radiation pulse duration from all particles, the length of the required uniform time grid T_u can be approximately chosen as

$$T_u \approx T_{\text{rad}}^{\text{bunch}} + T_{\text{rad}} \approx \frac{l_{b,x}}{\gamma c_0} + \frac{l_{b,y}}{\gamma c_0} + \frac{l_{b,z}}{c_0} + \frac{T_{\text{laser}}}{2\gamma^2}. \tag{16}$$

Table 1 lists the values for T_u computed from Eq. (16) for different parameter settings. We also provide values for T_u from a trial simulation to verify the theoretical estimates. Once $t_u^{\min}$ and T_u are known, $t_u^{\max} = t_u^{\min} + T_u$ can be immediately determined.

4.1. Interpolation

In the previous subsection, we discussed how to choose the bounds of a uniform time grid in order to determine the temporal positions for the computation of the total radiation field. Next, we interpolate the particles' fields at different temporal (advanced) positions to the uniform grid by piecewise linear interpolation (see Fig. 6).

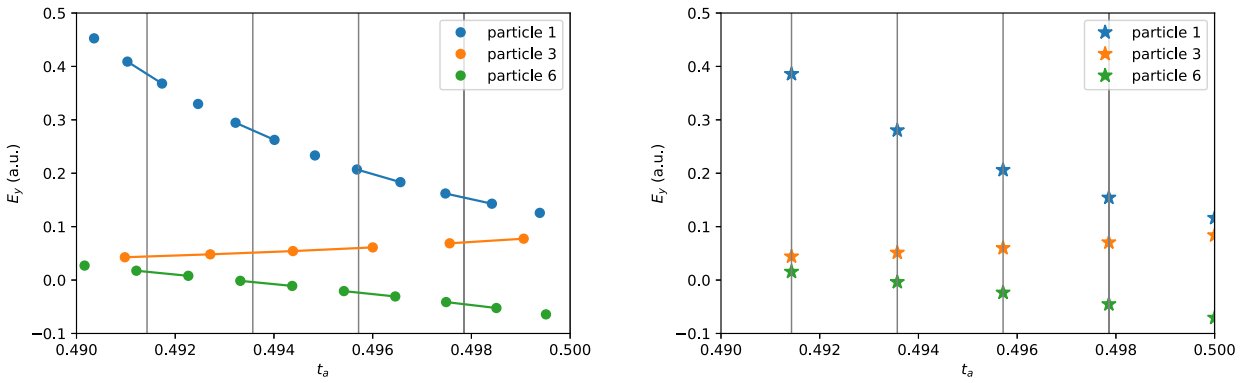

(a) local linear interpolation (b) resulting grid values

Fig. 6. Linear interpolation scheme for the temporal radiation profile. The gray vertical lines mark the position of the uniform time grid points. The round points in (a) connected by line segments are used for interpolation. (b) shows the result after interpolation. The stars indicate the values of the interpolated field.

To apply linear interpolation, one needs the arrival times and corresponding radiation fields from each particle at the previous and current time steps. This might suggest that we need two memory buffers for storing the field information of adjacent time steps. However, we actually only need one memory buffer to store the field information of the previous step. In every time step, we compute the field in the current time step for each particle and interpolate with the field stored in the memory buffer. Once the interpolated field and the corresponding position at the uniform time grid are calculated, the interpolated field is superimposed to the value at the array for storing the total radiation field of the particles. The complete procedure is described in Algorithm 2 (for a single observation direction $\boldsymbol{n}$).

Algorithm 2: Proposed Time-Domain Method.

Initialization:
- $\boldsymbol{E}_{tot}(\boldsymbol{n}, t_u) \leftarrow 0$ (total field from all particles over a uniform grid with points t_u)
- $t_b^k(\boldsymbol{n}) \leftarrow 0$ (buffer for storing of the field's arrival time of particle k computed at previous step)
- $\boldsymbol{E}_b^k(\boldsymbol{n}) \leftarrow 0$ (buffer for storing the arrival field of particle k computed at previous time step)

for *simulation step* i **do**
- **for** *particle* k **do**
  - update trajectory
  - compute $t_a^k(\boldsymbol{n})$ and $E^k(\boldsymbol{n}, t_a^k)$
  - **for** $t_u : t_b^k(\boldsymbol{n}) < t_u \leq t_a^k(\boldsymbol{n})$ **do**
    - $\boldsymbol{E}_{tot}(\boldsymbol{n}, t_u) \leftarrow \boldsymbol{E}_{tot}(\boldsymbol{n}, t_u) + \boldsymbol{E}_b^k(\boldsymbol{n}) \frac{t_a^k(\boldsymbol{n}) - t_u}{t_a^k(\boldsymbol{n}) - t_b^k(\boldsymbol{n})} + \boldsymbol{E}^k(\boldsymbol{n}, t_a^k) \frac{t_u - t_b^k(\boldsymbol{n})}{t_a^k(\boldsymbol{n}) - t_b^k(\boldsymbol{n})}$
- $t_b^k(\boldsymbol{n}) \leftarrow t_a^k(\boldsymbol{n})$
- $\boldsymbol{E}_b^k(\boldsymbol{n}) \leftarrow \boldsymbol{E}^k(\boldsymbol{n}, t_a^k)$

4.2. Parallelization

Before discussing parallelization, we briefly introduce key data structures used in the code development. Here, the memory cost is measured by the number of floating-point numbers to be stored.

Beam: A structure to store the state of motion (position, momentum, velocity and acceleration) for a bunch of particles at a specific time. For a particle bunch with N_p particles in three dimensional space, $12N_p$ floating-point numbers are required.

Sensor: A sensor records the total radiation field from a bunch of particles over the uniform time grid. For N_{T_u} uniform time grid points, $3N_{T_u}$ floating-point numbers are required. In addition, each particle's radiation arrival time and radiation field are also stored in a memory buffer which requires $4N_p$ floating-point numbers.

Detector: A detector contains N_{obs} sensors and each sensor has a different observation position. The memory cost for the detector is thus $N_{\text{obs}}(4N_p + 3N_{T_u})$ floating-point numbers.

There are at least two possible parallelization schemes for the simulation, see Fig. 7. One is beam parallelization in which the particle bunch is divided into several small bunches and each small bunch is assigned to an MPI process. Each process creates its own detector object which receives the radiation from a small bunch. At the end of the simulation, the radiation

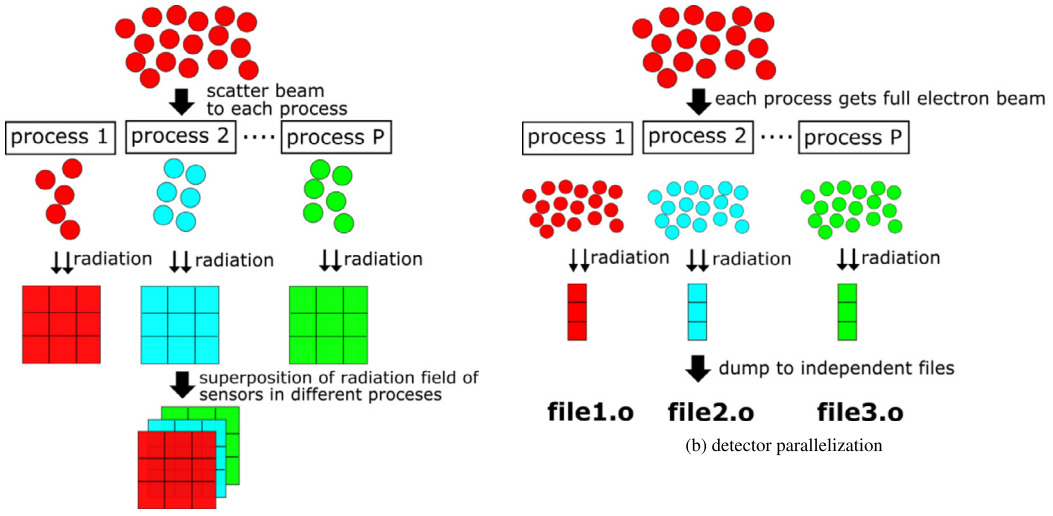

(a) beam parallelization

(b) detector parallelization

Fig. 7. Two possible parallelization schemes: (a) beam parallelization and (b) detector parallelization.

data in each detector object is superimposed to the radiation data in the detector object created by the master task. The other possible scheme is detector parallelization where a global sensor in the detector is divided into several local detectors. In the beginning of the simulation, each process creates a copy of the entire electron bunch and a local detector consisting of a subset of sensors from the global detector. During the simulation, the local detector receives the radiation from the copy of the entire electron bunch owned by each process. At the end of the simulation, each process dumps the data from its local detector separately.

The simulation of ICS can involve a large number of particles and sensors. Therefore, the memory requirement per process for both parallelization schemes is an important consideration. For beam parallelization, the memory cost per process is

$$M_{\text{beam}}(P, N_p, N_{\text{obs}}, N_{T_u}) = 12\frac{N_p}{P} + N_{\text{obs}}\left(4\frac{N_p}{P} + 3N_{T_u}\right)$$

where P is the number of computer processes. For detector parallelization, the memory cost per process is

$$M_{\text{detector}}(P, N_p, N_{\text{obs}}, N_{T_u}) = 12N_p + \frac{N_{\text{obs}}}{P}\left(4N_p + 3N_{T_u}\right).$$

In order to determine which scheme has lower memory cost, we define the function

$$\begin{aligned}\phi(P, N_p, N_{\text{obs}}, N_{T_u}) &\equiv \frac{M_{\text{beam}}(P, N_p, N_{\text{obs}}, N_{T_u})}{M_{\text{detector}}(P, N_p, N_{\text{obs}}, N_{T_u})} = \frac{12\frac{N_p}{P} + N_{\text{obs}}\left(4\frac{N_p}{P} + 3N_{T_u}\right)}{12N_p + \frac{N_{\text{obs}}}{P}\left(4N_p + 3N_{T_u}\right)} \\ &= 1 + \frac{3\left(1 - \frac{1}{P}\right)\left(N_{\text{obs}}N_{T_u} - 4N_p\right)}{12N_p + \frac{N_{\text{obs}}}{P}\left(4N_p + 3N_{T_u}\right)}. \end{aligned} \tag{17}$$

If $\phi > 1$, detector parallelization has a lower memory footprint and otherwise beam parallelization. Since the factor $(1-1/P)$ in the enumerator and all terms in the denominator of the second term are positive, we conclude that

$$\phi(P, N_p, N_{\text{obs}}, N_{T_u}) \quad \begin{cases} \geq 1 & \text{if } N_{\text{obs}}N_{T_u} - 4N_p \geq 0, \\ < 1 & \text{else.} \end{cases} \tag{18}$$

Therefore, the ratio $N_{\text{obs}}N_{T_u}/(4N_p)$ determines which parallelization scheme is more favorable in terms of memory consumption.

The number of particles N_p can be computed from the total charge of the electron bunch. The number of uniform grid points N_{T_u} should be chosen according to the Nyquist theorem

$$N_{T_u} = 2\frac{\omega_{\max}}{\Delta\omega}. \tag{19}$$

Here, $\omega_{\max}$ is the maximum radiation angular-frequency we want to observe which can be estimated by

$$\omega_{\max} = 4\gamma^2\omega_0 \tag{20}$$

Table 2
The ratio $4N_p/N_{T_u}$ ratio for different experimental projects. Here, the electron beam transverse sizes l_x and l_y are not considered in the evaluation of N_{T_u} since their contribution is minor for a high energy electron beam.

project name	beam energy (MeV)	l_z (μm)	charge (pC)	T_{laser} (ps)	λ_0 (μm)	$4N_p/N_{T_u}$
AXSIS [7]	19.5	2.9	1	1	1	714.3
ODU CLS [25,26]	25	382	10	1.57	1	34.2
ASU CXFEL [10]	35	1.5	1	1.5	1.03	443.5
ASU CXLS [6]	40	147	100	3.0	1.03	357.1
XFI [11]	65.9	3	10	1.7	0.8	498.8
MuLCS [12]	45	15000	1000	26	1.064	28.6
ThomX [13,14]	70	6000	1000	11.75	1.03	28.6

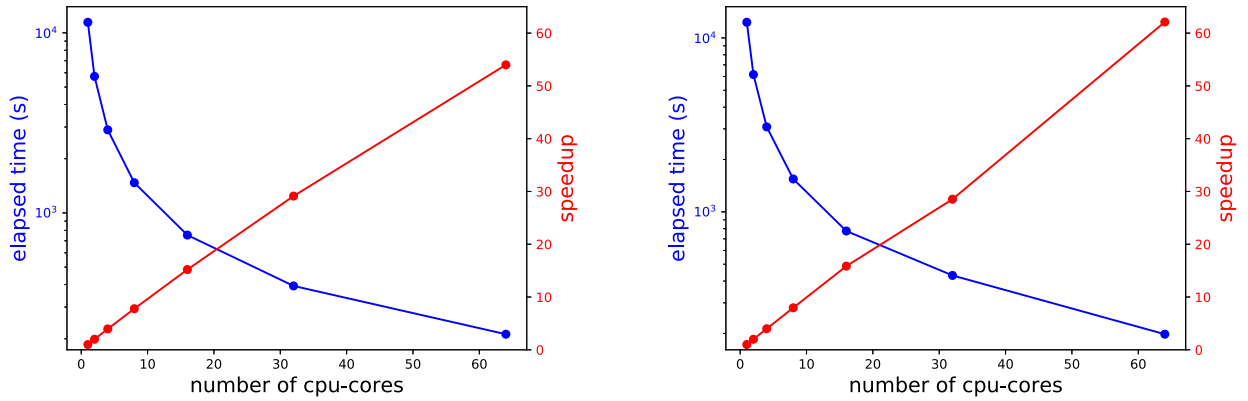

(a) Time-domain method

(b) Frequency-domain method

Fig. 8. Parallel performance for: (a) proposed time-domain simulation with $N_p = 10^5$, $N_{\text{obs}} = 1024$ and $N_{T_u} = 10^4$; (b) frequency-domain simulation with $N_p = 1024$, $N_{\text{obs}} = 64$ and $N_\omega = 500$.

for a typical ICS problem where ω_0 is the angular-frequency of the counter-propagating laser. The resolution for the angular-frequency is determined by the duration of the total radiation pulse from particles

$$\Delta\omega = \frac{2\pi}{T_u}. \tag{21}$$

Combining Eq. (19), Eq. (20), Eq. (21) and Eq. (16), we can estimate

$$N_{T_u} \approx 8\gamma^2 \left(\frac{l_{b,x}}{\gamma\lambda_0} + \frac{l_{b,y}}{\gamma\lambda_0} + \frac{l_{b,z}}{\lambda_0} + \frac{c_0 T_{\text{laser}}}{2\gamma^2\lambda_0} \right)$$

where the identity $\omega_0 = 2\pi c_0/\lambda_0$ is used.

In Table 2, we use parameters from different experimental projects of ICS sources to compute the ratio $4N_{T_p}/N_{T_u}$ which is the number of observers where both parallelization schemes break even ($\phi = 1$). Hence, according to (18), for a larger number of observers, detector parallelization is preferable whereas a smaller number of observers should be computed with beam parallelization. In general, we need at least a few thousand observation angles (i.e., $N_{\text{obs}} > 1000$) to sufficiently resolve the radiation angular distribution. Therefore, detector parallelization is more favorable and is thus implemented in the solver.

4.3. Implementation

We use C++ and MPI to implement the time-domain algorithm and the detector parallelization scheme described in this section. The parallel performance for the code is demonstrated in Fig. 8(a). For comparison, the parallel performance of our implementation of the frequency-domain method is also given in Fig. 8(b). A parallelized post-processing code written in Julia and MPI.jl is used to transform the time-domain field to the radiation spectra. The two solvers can be accessed via https://doi.org/10.5281/zenodo.5139340.

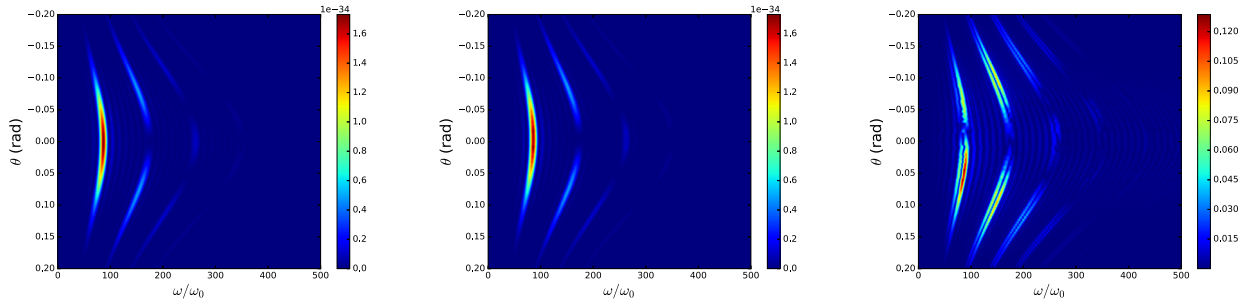

(a) theory (b) time-domain method (c) relative error

Fig. 9. Demonstration of the accuracy of the time-domain method. The radiation spectral-angular distribution is computed by (a) theory and (b) the time-domain method for the configuration stated in section 5.1. The relative error (c) is computed by Eq. (22).

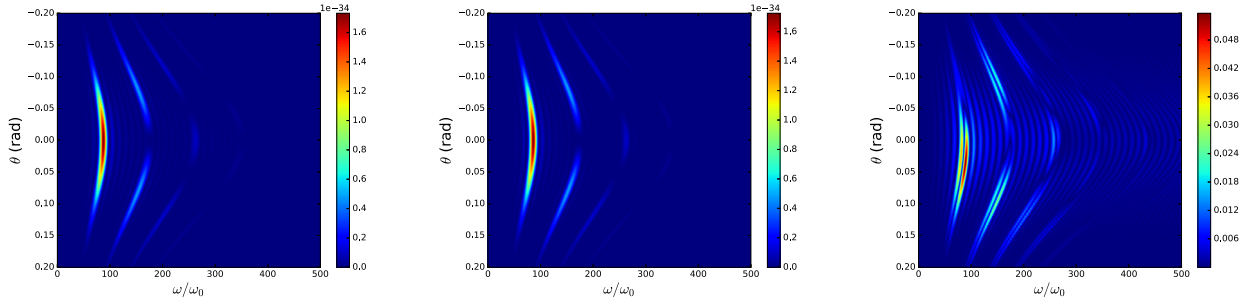

(a) theory (b) frequency-domain method (c) relative error

Fig. 10. Demonstration of the accuracy of the frequency-domain method. The radiation spectral-angular distribution is computed by (a) theory and (b) the frequency-domain method for the configuration stated in section 5.1. The relative error (c) is computed by Eq. (22).

5. Numerical comparison of the time-domain and frequency-domain methods

5.1. Accuracy

To compare the accuracy of the radiation spectra computed by both methods, we measure the component-wise relative error

$$\text{error}(\omega,\theta) = \text{abs}\left(\left.\frac{dI}{d\omega d\Omega}\right|_{\text{simulation}} - \left.\frac{dI}{d\omega d\Omega}\right|_{\text{theory}}\right) / \max\left(\left.\frac{dI}{d\omega d\Omega}\right|_{\text{theory}}\right). \tag{22}$$

between the theoretical and computed results [19]. The theoretical result is computed by the formula proposed by Esarey et al. [8] which considers the radiation spectral-angular distribution from a single particle interacting with a finite number of periods of a sinusoidal electromagnetic wave.

We perform a single particle simulation in which a particle moves with initial energy $\gamma = 5$ in the $+z$ direction and collides with 7 periods of a counter-propagating sinusoidal wave. The radiation is collected in observation directions in the y-z plane (i.e., $\theta_x = 0$ and $\theta_y = \theta$ in Fig. 5). The radiation spectral-angular distribution and the corresponding errors computed by Eq. (22) are illustrated in Fig. 9 for the time-domain method and in Fig. 10 for the frequency-domain method.

In addition, the maximum and mean values of normalized errors for the radiation spectral-angular distribution with different numbers of frequency points N_ω and different numbers of observation angles N_θ are shown in Table 3 and Table 4, respectively. The relative error over the full spectral-angular distribution for the time-domain method and frequency-domain method has an asymmetric distribution with respect to $\theta = 0$. This is due to the discretized particle trajectory in the simulation and can be reduced by decreasing the step size for solving the particle trajectory [19]. From Table 4 and Table 3, we see that both methods achieve an acceptable relative error and that the time-domain method reaches the same level of accuracy as the frequency-domain method by increasing the number of observation points.

5.2. Performance

We will now discuss the computational complexity of the two schemes with respect to the following parameters:

Table 3
Normalized relative error of the time-domain method (TDM) and the frequency-domain method (FDM) for different numbers of frequency points.

$N_{\text{obs}} = 101$	$N_\omega = 5 \times 10^3$	$N_\omega = 1 \times 10^4$	$N_\omega = 2 \times 10^4$
TDM			
$\max(\text{error}(\omega, \theta))$	1.287×10^{-1}	1.290×10^{-1}	1.291×10^{-1}
$\text{mean}(\text{error}(\omega, \theta))$	3.520×10^{-3}	3.522×10^{-3}	3.524×10^{-3}
FDM			
$\max(\text{error}(\omega, \theta))$	5.366×10^{-2}	5.366×10^{-2}	5.366×10^{-2}
$\text{mean}(\text{error}(\omega, \theta))$	1.589×10^{-3}	1.589×10^{-3}	1.580×10^{-3}

Table 4
Normalized relative error of the time-domain method (TDM) and the frequency-domain method (FDM) for different numbers of observation points.

$N_\omega = 5 \times 10^3$	$N_{\text{obs}} = 101$	$N_{\text{obs}} = 201$	$N_{\text{obs}} = 401$
TDM			
$\max(\text{error}(\omega, \theta))$	1.291×10^{-1}	8.587×10^{-2}	6.609×10^{-2}
$\text{mean}(\text{error}(\omega, \theta))$	3.524×10^{-3}	2.175×10^{-3}	1.547×10^{-3}
FDM			
$\max(\text{error}(\omega, \theta))$	5.366×10^{-2}	5.366×10^{-2}	5.366×10^{-2}
$\text{mean}(\text{error}(\omega, \theta))$	1.580×10^{-3}	1.596×10^{-3}	1.599×10^{-3}

N_s the number of simulation time steps,
N_p the number of particles,
N_{obs} the number of observers,
L_t the operation count to compute the advanced time t_a, see Eq. (5),
L_f the operation count to evaluate the radiation field, see Eq. (4),
L_I the operation count to interpolate the particle field,
N_{T_u} the number of grid points of the uniform time grid,
N_ω the number of grid points of the uniform frequency grid,
L_ω the operation count to evaluate a particle's contribution in the frequency-domain method, see Eq. (10).

The total operation count for the time-domain method is given by

$$\text{OP}_t = \text{const} \cdot N_s \cdot N_p \cdot N_{\text{obs}} \cdot (L_t + L_f + L_I) + \text{const} \cdot N_{\text{obs}} \cdot N_{T_u} \cdot \log N_{T_u}, \tag{23}$$

whereas for the frequency-domain method we have

$$\text{OP}_\omega = \text{const} \cdot N_s \cdot N_p \cdot N_{\text{obs}} \cdot N_\omega \cdot L_\omega. \tag{24}$$

The second term in the operation count for the time-domain method stems from an additional post-processing phase in which the radiation data on the uniform time grid is transformed to the frequency-domain by the FFT algorithm in order to obtain the radiation spectra. To easily measure the performance, we define a wall-clock time model for both the time-domain and frequency-domain method. If the memory latency is neglected and the wall-clock time only depends on the operation count of the method, i.e., OP_t and OP_ω, the wall-clock time for the time-domain method can be split into the two parts

$$W_t^1(N_s, N_p, N_{\text{obs}}) = C_t^1 \cdot N_s \cdot N_p \cdot N_{\text{obs}}, \qquad W_t^2(N_{\text{obs}}, N_{T_u}) = C_t^2 \cdot N_{\text{obs}} \cdot N_{T_u} \cdot \log N_{T_u},$$

and the wall-clock time for the frequency-domain method is denoted by

$$W_\omega(N_s, N_p, N_{\text{obs}}, N_\omega) = C_\omega \cdot N_s \cdot N_p \cdot N_{\text{obs}} \cdot N_\omega.$$

The leading constants translate the operation count into wall-clock time and depend on the implementation and computer architecture (*e.g.*, implementation details, operating system, hardware, and compiler, which are not our primary concerns in this study). Since our analysis only involves the ratio of the constants, the dependency of the computer architecture at which the simulation is performed will most likely be canceled out. We can determine the leading constants for both models by the regression of several benchmark runs of both methods (Fig. 11 and Fig. 12) and obtain

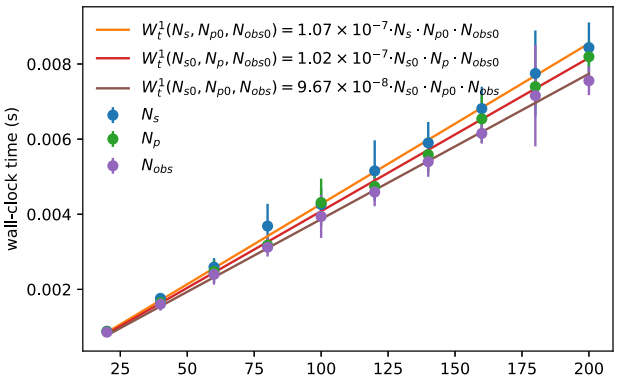

(a) Fitting of W_t^1

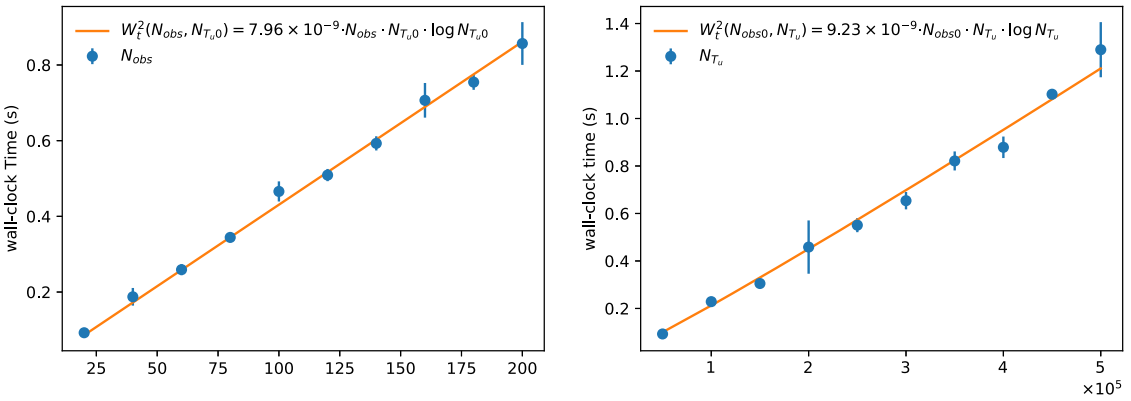

(b) Fitting of W_t^2

Fig. 11. Fitting of (a) W_t^1 and (b) W_t^2 by splitting the multi-variate problem to multiple single-variate fitting problems. Here, $N_{s0} = 20$, $N_{p0} = 20$, $N_{obs0} = 20$ and $N_{T_u 0} = 5 \times 10^4$. Each data point represents the average wall-clock time of 50 runs. The leading constants $C_t^1 = 1.02 \times 10^{-7}$ and $C_t^2 = 8.61 \times 10^{-9}$ are determined as the averages of all respective single-variate fitting constants.

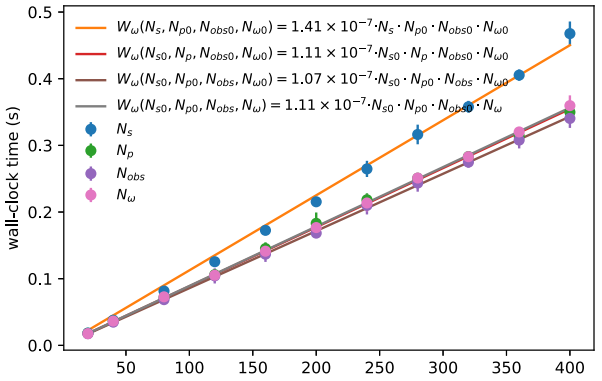

Fig. 12. Fitting of W_ω by splitting the multi-variate problem to multiple single-variate fitting problems. $N_{s0} = 20$, $N_{p0} = 20$, $N_{obs0} = 20$ and $N_{\omega 0} = 20$. The leading constant $C_\omega = 1.17 \times 10^{-7}$ is determined as the average of all single-variate fitting constants.

$$C_t^1 = 1.02 \times 10^{-7}, \quad C_t^2 = 8.61 \times 10^{-9}, \quad C_\omega = 1.17 \times 10^{-7} \tag{25}$$

for our implementation and computer architecture.

The wall-clock time ratio of the time-domain and frequency-domain method is given by

$$\frac{W_t^1 + W_t^2}{W_\omega} = \frac{C_t^1 \cdot N_s \cdot N_p + C_t^2 \cdot N_{T_u} \cdot \log N_{T_u}}{C_\omega \cdot N_s \cdot N_p \cdot N_\omega}. \tag{26}$$

If we set $N_{T_u} = 2N_\omega$ for the reason of sampling theory, the ratio simplifies to

$$\frac{W_t^1 + W_t^2}{W_\omega} = \frac{C_t^1}{C_\omega}\frac{1}{N_\omega} + \frac{C_t^2}{C_\omega}\frac{2}{N_s N_p}\log 2N_\omega.$$

The ratio is greater than one (*i.e.*, the frequency-domain method outperforms the time-domain method) if

$$N_\omega > \frac{1}{2}\exp\left(\frac{1}{2}\frac{C_\omega}{C_t^2}\cdot N_s \cdot N_p\right),$$

which is typically not satisfied with the parameters from practical scenarios. For a simulation of a 1pC particle bunch colliding with a 1 μm laser pulse with $1ps$ duration, the required simulation parameters are $N_s = 6000$ (0.167 femtosecond per time step) and $N_p = 6.25 \times 10^6$. In this case, using the experimentally fitted constants in (25), the criterion for the frequency-domain method to outperform the time-domain method is $N_\omega > 0.5\exp(2.5479 \cdot 10^{11}) = \mathcal{O}\left(10^{10^{11}}\right)$.

In the previous discussion, we assumed that the number of time points for the time-domain method is twice the number of frequency points for the frequency-domain method which originated from the assumption that the frequency resolutions for both methods are the same. However, this condition is not necessary in practice. For the time-domain method, the upper limit of $\Delta\omega$ is restrictively determined (due to the sampling theorem) by the total radiation pulse duration. It could be possible that the upper limit of $\Delta\omega$ is far less than the actual resolution that we need to study a problem. For the frequency-domain method, on the other hand, there is no such limitation. The resolution $\Delta\omega$ can be chosen arbitrarily. The bandwidth $\overline{\omega}$ of the maximum frequency which refers to the first harmonic frequency of ICS is [8]

$$\overline{\omega} = \frac{\lambda_0}{c_0 T_{\text{laser}}}\omega_{\max}.$$

Thus, when applying the frequency-domain method,

$$\Delta\omega = \frac{1}{N_{\overline{\omega}}}\frac{\lambda_0}{c_0 T_{\text{laser}}}\omega_{\max} \quad \text{and} \quad N_\omega = N_{\overline{\omega}}\frac{c_0 T_{\text{laser}}}{\lambda_0}, \tag{27}$$

where $N_{\overline{\omega}}$ is the number of grid points needed for $\overline{\omega}$. To find a condition under which the time-domain method is slower than the frequency-domain method, Eq. (26) can be expressed as

$$C_t^2 \cdot N_{T_u} \cdot \log N_{T_u} > (C_\omega \cdot N_\omega - C_t^1) N_s \cdot N_p$$

and rewritten by

$$N_{T_u} \cdot \log N_{T_u} > \frac{C_\omega}{C_t^2} N_\omega \cdot N_s \cdot N_p. \tag{28}$$

Here, C_t^1 should be of the same order of magnitude as C_ω and is negligible compared to $C_\omega N_\omega$. From Eq. (28), we can have two immediate conclusions:

1. The time-domain method is favorable when the laser pulse duration or the charge of the particle beam is large.
2. The frequency-domain method is better when a particle beam with high energy or long bunch length is considered.

In addition, the factor C_ω / C_t^2 in Eq. (28) can also have significant contribution. The value of C_ω depends not only on the performance of hardware but also on the algorithm for solving the particle trajectory. If a more sophisticated algorithm is utilized (*e.g.*, particle-in-cell method [17,18]), the time-domain method may become more favorable. In Table 5, we demonstrate the ratio of $N_{T_u} \cdot \log N_{T_u}$ and $C_\omega / C_t^2 \cdot N_\omega \cdot N_s \cdot N_p$ for different experimental projects. We can observe that the time-domain method is still faster than the frequency-domain method even if we choose N_ω so that $\Delta\omega$ fulfills Eq. (27).

Although the TDM outperforms the FDM for large particle numbers typically used in ICS sources, it is interesting to study the transition where the TDM outperforms the FDM for low particle numbers since ICS is also used in other applications. To numerically demonstrate the situation where FDM outperforms the TDM, we consider a bunch of particles uniformly distributed along the longitudinal direction with length of 100 μm. This particle bunch interacts with 5 periods of a 1 μm sinusoidal wave. We measure the elapsed time for simulation with different numbers of particles by both TDM and FDM. The result is demonstrated in Fig. 13, the FDM wins when $N_p \leq 40$ and the TDM wins when $N_p > 40$.

Although the performance model is verified by the execution times in serial, our conclusions can be extended to the scenario with parallelization (i.e. with detector parallelization) in which the total operation counts for the time-domain and frequency-domain methods can be written as OP_t/P and OP_ω/P, resp.

Table 5
The ratio of $N_{T_u} \cdot \log N_{T_u}$ and $C_\omega / C_t^2 \cdot N_\omega \cdot N_s \cdot N_p$ for different experimental projects is computed. Here, the electron beam transverse size l_x and l_y are not considered in the evaluation of N_{Tu} as their contribution is minor for a high energy electron beam. The reference of each experimental project can be found in Table 2.

AXSIS	ODU CLS	ASU CXFEL	ASU CXLS	XFI	MuLCS	ThomX
4.75×10^{-7}	6.09×10^{-9}	3.77×10^{-10}	1.69×10^{-10}	1.89×10^{-10}	3.91×10^{-11}	1.79×10^{-10}

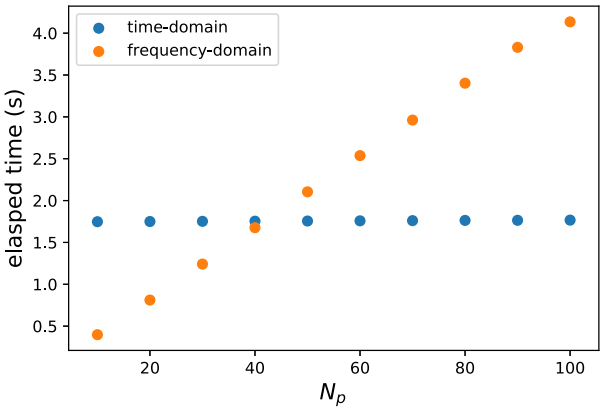

Fig. 13. Elapsed times for the simulation ($N_s = 100$) with different numbers of particles (N_p) by the time-domain method ($N_{Tu} = 1.28 \times 10^6$) and the frequency-domain method ($N_\omega = 100$). Each data point is the average elapsed time from 50 simulation runs. In this case, the frequency-domain method outperforms the time-domain method when $N_p \leq 40$.

In this study, the space charge force between charged particles has not been included when solving the dynamics of charged particles. However, it might be significant for some light sources from particle beams with relatively low γ (*e.g.* AXSIS [7]), and will be the subject of future work.

Declaration of competing interest

The authors declare that they have no known competing financial interests or personal relationships that could have appeared to influence the work reported in this paper.

Acknowledgement

The authors acknowledge the support by DASHH (Data Science in Hamburg - HELMHOLTZ Graduate School for the Structure of Matter) with the Grant-No. HIDSS-0002. This research was supported in part through the Maxwell computational resources operated at Deutsches Elektronen-Synchrotron (DESY), Hamburg, Germany.

References

[1] C. Bostedt, S. Boutet, D.M. Fritz, Z. Huang, H.J. Lee, H.T. Lemke, A. Robert, W.F. Schlotter, J.J. Turner, G.J. Williams, Linac coherent light source: the first five years, Rev. Mod. Phys. 88 (1) (2016) 015007, https://doi.org/10.1103/RevModPhys.88.015007, https://link.aps.org/doi/10.1103/RevModPhys.88.015007.

[2] C. Pellegrini, The development of XFELs, Nat. Rev. Phys. 2 (7) (2020) 330–331, https://doi.org/10.1038/s42254-020-0197-1, http://www.nature.com/articles/s42254-020-0197-1.

[3] G.A. Krafft, G. Priebe, Compton sources of electromagnetic radiation, Rev. Accel. Sci. Technol. 03 (01) (2010) 147–163, https://doi.org/10.1142/S1793626810000440, https://www.worldscientific.com/doi/abs/10.1142/S1793626810000440.

[4] K. Ta Phuoc, S. Corde, C. Thaury, V. Malka, A. Tafzi, J.P. Goddet, R.C. Shah, S. Sebban, A. Rousse, All-optical Compton gamma-ray source, Nat. Photonics 6 (5) (2012) 308–311, https://doi.org/10.1038/nphoton.2012.82, http://www.nature.com/articles/nphoton.2012.82.

[5] D.H. Bilderback, P. Elleaume, E. Weckert, Review of third and next generation synchrotron light sources, J. Phys. B, At. Mol. Opt. Phys. 38 (9) (2005) S773–S797, https://doi.org/10.1088/0953-4075/38/9/022, https://iopscience.iop.org/article/10.1088/0953-4075/38/9/022.

[6] W. Graves, J. Bessuille, P. Brown, S. Carbajo, V. Dolgashev, K.-H. Hong, E. Ihloff, B. Khaykovich, H. Lin, K. Murari, E. Nanni, G. Resta, S. Tantawi, L. Zapata, F. Kärtner, D. Moncton, Compact x-ray source based on burst-mode inverse Compton scattering at 100 kHz, Phys. Rev. Spec. Top., Accel. Beams 17 (12) (2014) 120701, https://doi.org/10.1103/PhysRevSTAB.17.120701, https://link.aps.org/doi/10.1103/PhysRevSTAB.17.120701.

[7] F. Kärtner, F. Ahr, A.-L. Calendron, H. Çankaya, S. Carbajo, G. Chang, G. Cirmi, K. Dörner, U. Dorda, A. Fallahi, A. Hartin, M. Hemmer, R. Hobbs, Y. Hua, W. Huang, R. Letrun, N. Matlis, V. Mazalova, O. Mücke, E. Nanni, W. Putnam, K. Ravi, F. Reichert, I. Sarrou, X. Wu, A. Yahaghi, H. Ye, L. Zapata, D. Zhang, C. Zhou, R. Miller, K. Berggren, H. Graafsma, A. Meents, R. Assmann, H. Chapman, P. Fromme, AXSIS: exploring the frontiers in attosecond X-ray science, imaging and spectroscopy, Nucl. Instrum. Methods Phys. Res., Sect. A, Accel. Spectrom. Detect. Assoc. Equip. 829 (2016) 24–29, https://doi.org/10.1016/j.nima.2016.02.080, https://linkinghub.elsevier.com/retrieve/pii/S0168900216002564.

[8] E. Esarey, S.K. Ride, P. Sprangle, Nonlinear Thomson scattering of intense laser pulses from beams and plasmas, Phys. Rev. E 48 (4) (1993) 3003–3021, https://doi.org/10.1103/PhysRevE.48.3003, https://link.aps.org/doi/10.1103/PhysRevE.48.3003.

[9] K. Deitrick, J. Delayen, G. Krafft, High average brilliance compact inverse Compton light source, in: Proc. of International Particle Accelerator Conference (IPAC'17), Copenhagen, Denmark, from May 14 – 19, 2017, no. 8 in International Particle Accelerator Conference, JACoW, Geneva, Switzerland, 2017, 2017, pp. 932–935, http://jacow.org/ipac2017/papers/mopva036.pdf.

[10] W. Graves, J. Chen, P. Fromme, M. Holl, K.-H. Hong, R. Kirian, C. Limborg-Deprey, L. Malin, D. Moncton, E. Nanni, K. Schmidt, J. Spence, M. Underhill, U. Weierstall, N. Zatsepin, C. Zhang, ASU compact XFEL, in: Proceedings of the 38th Int. Free Electron Laser Conf. FEL2017, JACoW, Geneva, Switzerland, ISBN 9783954501793, 2018, 4 pages, 0.925 MB, artwork Size: 4 pages, 0.925 MB, http://jacow.org/fel2017/doi/JACoW-FEL2017-TUB03.html.

[11] T. Brümmer, A. Debus, R. Pausch, J. Osterhoff, F. Grüner, Design study for a compact laser-driven source for medical x-ray fluorescence imaging, Phys. Rev. Accel. Beams 23 (3) (2020) 031601, https://doi.org/10.1103/PhysRevAccelBeams.23.031601, https://link.aps.org/doi/10.1103/PhysRevAccelBeams.23.031601.

[12] B. Günther, R. Gradl, C. Jud, E. Eggl, J. Huang, S. Kulpe, K. Achterhold, B. Gleich, M. Dierolf, F. Pfeiffer, The versatile X-ray beamline of the Munich compact light source: design, instrumentation and applications, J. Synchrotron Radiat. 27 (5) (2020) 1395–1414, https://doi.org/10.1107/S1600577520008309, muLCS (ring), https://scripts.iucr.org/cgi-bin/paper?S1600577520008309.

[13] A. Variola, J. Haissinski, A. Loulergue, F. Zomer, ThomX Technical Design Report, Tech. rep., ThomX - Dept. Accelerateurs, 2014, http://hal.in2p3.fr/in2p3-00971281.

[14] K. Dupraz, M. Alkadi, M. Alves, L. Amoudry, D. Auguste, J.-L. Babigeon, M. Baltazar, A. Benoit, J. Bonis, J. Bonenfant, C. Bruni, K. Cassou, J.-N. Cayla, T. Chabaud, I. Chaikovska, S. Chance, V. Chaumat, R. Chiche, A. Cobessi, P. Cornebise, O. Dalifard, N. Delerue, R. Dorkel, D. Douillet, J.-P. Dugal, N. El Kamchi, M. El Khaldi, E. Ergenlik, P. Favier, M. Fernandez, A. Gamelin, J.-F. Garaut, L. Garolfi, P. Gauron, F. Gauthier, A. Gonnin, D. Grasset, E. Guerard, H. Guler, J. Haissinski, E. Herry, G. Iaquaniello, M. Jacquet, E. Jules, V. Kubytskyi, M. Langlet, T. Le Barillec, J.-F. Ledu, D. Leguidec, B. Leluan, P. Lepercq, F. Letellier-Cohen, R. Marie, J.-C. Marrucho, A. Martens, C. Mageur, G. Mercadier, B. Mercier, E. Mistretta, H. Monard, A. Moutardier, O. Neveu, D. Nutarelli, M. Omeich, Y. Peinaud, Y. Petrilli, M. Pichet, E. Plaige, C. Prévost, P. Rudnicky, V. Soskov, M. Taurigna-Quéré, S. Trochet, C. Vallerand, O. Vitez, F. Wicek, S. Wurth, F. Zomer, P. Alexandre, R. Ben El Fekih, P. Berteaud, F. Bouvet, R. Cuoq, A. Diaz, Y. Dietrich, M. Diop, D. Pedeau, E. Dupuy, F. Marteau, F. Bouvet, A. Gamelin, D. Helder, N. Hubert, J. Veteran, M. Labat, A. Lestrade, A. Letrésor, R. Lopes, A. Loulergue, M. Louvet, M. Louvet, P. Marchand, M. El Ajjouri, D. Muller, A. Nadji, L. Nadolski, R. Nagaoka, S. Petit, J.-P. Pollina, F. Ribeiro, M. Ros, J. Salvia, S. Bobault, M. Sebdaoui, R. Sreedharan, Y. Bouanai, J.-L. Hazemann, J.-L. Hodeau, E. Roy, P. Jeantet, J. Lacipière, P. Robert, J.-M. Horodynski, H. Bzyl, C. Chapelle, M. Biagini, P. Walter, A. Bravin, W. Del Net, E. Lahéra, O. Proux, H. Elleaume, E. Cormier, The ThomX ICS source, Phys. Open 5 (2020) 100051, https://doi.org/10.1016/j.physo.2020.100051, thomx (Ring), https://linkinghub.elsevier.com/retrieve/pii/S2666032620300387.

[15] A.G.R. Thomas, Algorithm for calculating spectral intensity due to charged particles in arbitrary motion, Phys. Rev. Spec. Top., Accel. Beams 13 (2) (2010) 020702, https://doi.org/10.1103/PhysRevSTAB.13.020702, https://link.aps.org/doi/10.1103/PhysRevSTAB.13.020702.

[16] J.T. Frederiksen, T. Haugbølle, M.V. Medvedev, Å. Nordlund, Radiation spectral synthesis of relativistic filamentation, Astrophys. J. 722 (1) (2010) L114–L119, https://doi.org/10.1088/2041-8205/722/1/L114, https://iopscience.iop.org/article/10.1088/2041-8205/722/1/L114.

[17] T. Haugbølle, J.T. Frederiksen, Å. Nordlund, PHOTON-PLASMA: a modern high-order particle-in-cell code, Phys. Plasmas 20 (6) (2013) 062904, https://doi.org/10.1063/1.4811384, http://aip.scitation.org/doi/10.1063/1.4811384.

[18] R. Pausch, H. Burau, M. Bussmann, J. Couperus, T. Cowan, A. Debus, A. Huebl, A. Irman, A. Köhler, U. Schramm, K. Steiniger, R. Widera, Computing angularly-resolved far field emission spectra in particle-in-cell codes using GPUs, in: Proceedings of the 5th Int. Particle Accelerator Conf. IPAC2014, ISBN 9783954501328, JACoW, Geneva Switzerland, 2014, 4 pages, 0.581 MB, artwork Size: 4 pages, 0.581 MB, http://jacow.org/IPAC2014/doi/JACoW-IPAC2014-MOPRI069.html.

[19] R. Pausch, A. Debus, R. Widera, K. Steiniger, A. Huebl, H. Burau, M. Bussmann, U. Schramm, How to test and verify radiation diagnostics simulations within particle-in-cell frameworks, Nucl. Instrum. Methods Phys. Res., Sect. A, Accel. Spectrom. Detect. Assoc. Equip. 740 (2014) 250–256, https://doi.org/10.1016/j.nima.2013.10.073, https://linkinghub.elsevier.com/retrieve/pii/S0168900213014642.

[20] R. Pausch, Electromagnetic Radiation from Relativistic Electrons as Characteristic Signature of their Dynamics, PhD Thesis, Technische Universität Dresden, Dec. 2012, https://doi.org/10.5281/zenodo.843510.

[21] A. Sell, F.X. Kärtner, Attosecond electron bunches accelerated and compressed by radially polarized laser pulses and soft-x-ray pulses from optical undulators, J. Phys. B, At. Mol. Opt. Phys. 47 (1) (2014) 015601, https://doi.org/10.1088/0953-4075/47/1/015601, https://iopscience.iop.org/article/10.1088/0953-4075/47/1/015601.

[22] D. Jackson, Classical Electrodynamics, Wiley, 1999.

[23] R.D. Ryne, Using a Lienard-Wiechert Solver to Study Coherent Synchrotron Radiation Effects, New York, 2013, p. 7.

[24] J.P. Boris, Relativistic plasma simulation-optimization of a hybrid code, in: Proc. Fourth Conf. Num. Sim. Plasmas, Naval Res. Lab, Wash. DC, 1970, pp. 3–67.

[25] K.E. Deitrick, Inverse Compton Light Source: A Compact Design Proposal, Old Dominion University, 2017.

[26] K. Deitrick, G. Krafft, B. Terzić, J. Delayen, High-brilliance, high-flux compact inverse Compton light source, Phys. Rev. Accel. Beams 21 (8) (2018) 080703, https://doi.org/10.1103/PhysRevAccelBeams.21.080703, old domin (Linac), https://link.aps.org/doi/10.1103/PhysRevAccelBeams.21.080703.